The missing piece: The $Ti_3C_2T_x$ MXene structure and its role in the outstanding reversibility as negative electrode in sodium ion batteries

Chiara Ferrara[a,b], Antonio Gentile[a], Stefano Marchionna[c], Irene Quinzeni[c], Martina Fracchia[d], Paolo Ghigna[d,e], Simone Pollastri[f], Clemens Ritter[g], Giovanni Maria Vanacore[a], Riccardo Ruffo[a,b]

a - Dipartimento di Scienza dei Materiali, Università di Milano Bicocca, 20125 Milano, Italy

b - National Reference Center for Electrochemical Energy Storage (GISEL) - Consorzio Interuniversitario Nazionale per la Scienza e Tecnologia dei Materiali (INSTM), 50121 Firenze, Italy

c - Ricerca sul Sistema Energetico - RSE S.p.A., Via R. Rubattino 54 - 20134 Milano, Italy

d - Dipartimento di Chimica, Università degli studi di Pavia, 27100, Pavia, Italy;

e - INSTM, Consorzio Interuniversitario per la Scienza e Tecnologia dei Materiali, I-50121 Firenze, Italy

f - Elettra-Sincrotrone Trieste, 34149, Basovizza, Trieste, Italy

g - Institut Laue-Langevin - 71 avenue des Martyrs CS 20156, 38042 Grenoble, Cedex 9, France;

ABSTRACT

This study proposes the full structural characterization of the most common MXene composition, $Ti_3C_2T_x$, which presents outstanding stability as anode for sodium ion batteries (100% of capacity retention after 530 cycles with charge efficiency > 99.7%). The structural investigation is carried out with a multi-technique approach that allows to explore both the short- and long- range structure, combining the analysis of X ray absorption spectroscopy, X-ray and neutron diffraction data, and TEM images. The diffraction data have been analyzed with the approach embodied in the Faults software, that accounts for the evaluation of extended defects, thus allowing to fit, for the first time, the MXene diffraction patterns. The analysis shows that the presence of static disorder on the termination sites induces a variability in the interlayer distance which affects the electrochemical properties.

The interest in the MXene family of 2D materials is experiencing an exponential growth thanks to the unique structural and functional properties[1,2]. MXene compounds are described by the general formula $M_{n-1}X_nT_x$ where M is a *d*-block transition metal (Sc, Ti, Zr, Hf, V, Nb, Ta, Cr, Mo…), X can be C, N, B, and T are termination groups (-O, -OH, -F, -Cl, -Br)[1,3]. MXenes are generally obtained by the corresponding MAX precursor through the etching of the A element (Al, Sn). However, despite this flexibility in the composition, about the 70% of the reported experimental data concerns the $Ti_3C_2T_x$ composition, since it can be obtained in various forms through accessible preparation routes[1,4,5]. The peculiar functional properties together with

the flexibility in the composition make the MXenes new promising materials for their exploitation in several fields such as catalysis[6], gas storage[7], sensing[8], drug delivery and cancer therapy[9], adsorption of heavy metals and radioactive pollutants[10] and electrochemical energy storage[1,4,11]. The $Ti_3C_2T_x$ is also the most appealing composition as anode material for Li-[12], Na-[13], and K-[14] rechargeable batteries and supercapacitors[15].

Beside the huge number of studies regarding the explorations of new compositions, substitutions, doping, hierarchic structures, and composites[3,16], some fundamental aspects of the structure of $Ti_3C_2T_x$ MXene are still unaddressed. Indeed: i) the composition and stoichiometry of the terminations are not completely controllable with the synthesis or post-synthetic treatments; ii) the actual composition is difficult to determine; and iii) the overall structure of $Ti_3C_2T_x$ has not been described yet. A full clarification of these aspects is the missing step in the understanding of the correlation between functional properties and the different synthetic routes and treatments[5,17,18-22]. Moreover, the understanding of the specific features can be the starting point for the improvement of the properties by controlling stoichiometry and structure.

One of the most interesting applications of the $Ti_3C_2T_x$ phase is as negative electrode in sodium ion batteries, especially considered that state-of-the-art hard carbon materials show poor cyclability and low rate capability[23]. The reversible intercalation of Na^+ ions in non-delaminated $Ti_3C_2T_x$ flakes was first demonstrated in 2015[24], and then optimized by our group[13]. We report here the long term cyclability performance of two $Ti_3C_2T_x$ MXenes obtained by different etching conditions from the Ti_3AlC_2 parental compound (MAX in the following): the $Ti_3C_2T_x$ obtained in 30% HF for 5 h (MXT-30) and the $Ti_3C_2T_x$ obtained in 5% HF for 24 h (MXT-5). The two compounds differ both in composition (for what concerns the T terminations) and structure, due to the different degree of disorder, as it will be discussed in more details in the following, and

show similar potential/capacity profiles in terms of both pseudo-capacitive behavior and first

cycle efficiency (Figure 1a), which is related to solid-electrolyte interphase (SEI) formation and

amount of sodium intercalated in the structure irreversibly[24]. To evaluate the practical

applications and to better highlight their difference in the electrochemical performances, we have

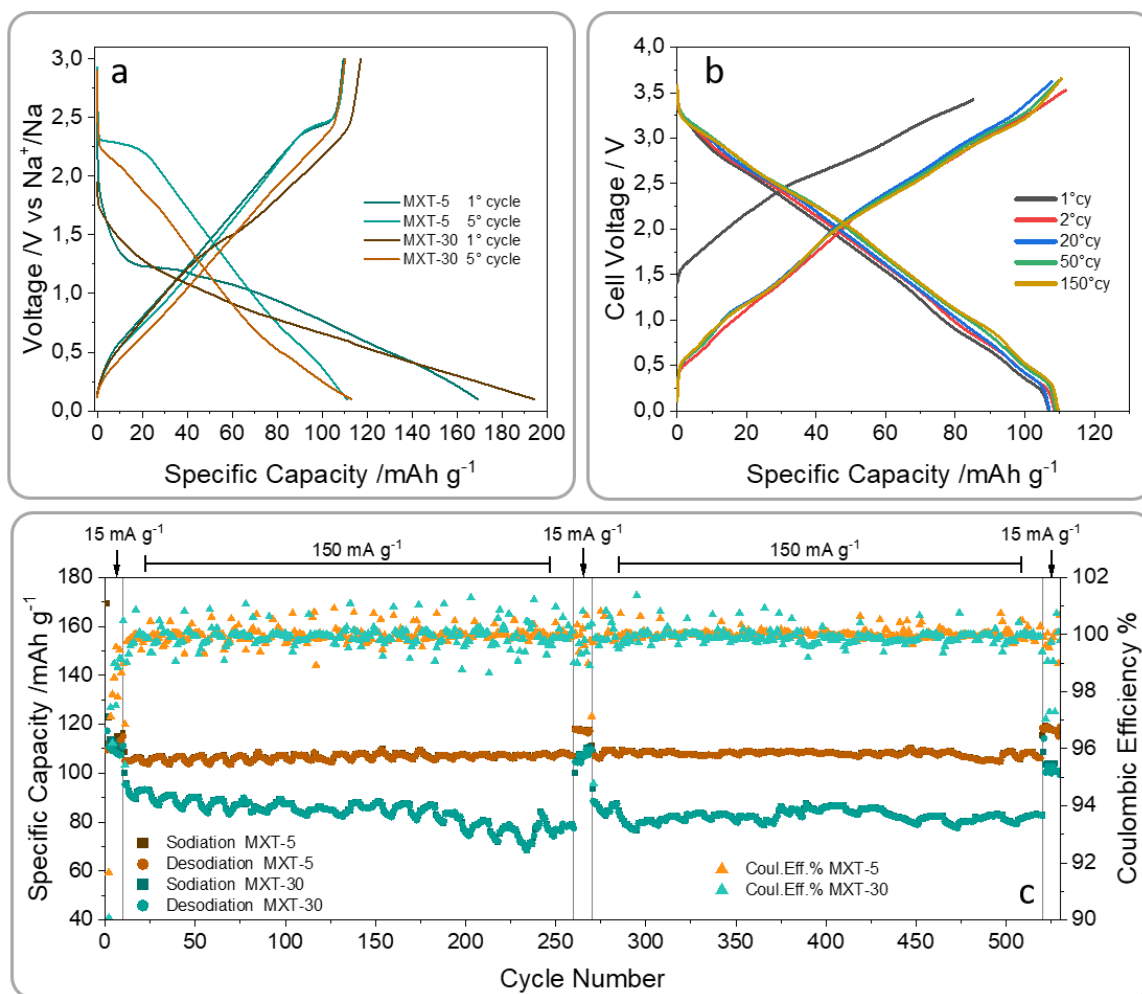cycled the two half cells for 530 cycles (Figure 1c).

Figure 1. Electrochemical performances of $Ti_3C_2T_x$ MXenes in Na-ion batteries (NIB). a) MXT-5 and MXT-30 charge discharge profiles at 15 mAg^{-1} in half cell vs. metallic Na using 1M NaPF$_6$ EC-DEC as electrolyte; b) Cell potential profile of a MTX-5 based NIB (galvanic chain MXT-5 │1M NaPF$_6$ EC-DEC │Na$_{0.44}$MnO$_2$) at 15 mAg^{-1}(both specific capacity and gravimetric current are calculated on the MXT-5 mass), c) long term cycling of MXT-5 and MXT-30 in half cell vs.

metallic Na. The applied cycling protocols are: 10 cycles at 15 mAg^{-1}, 250 cycles at 150 mAg^{-1}, 10 cycles at 15 mAg^{-1}, 250 cycles at 150 mAg^{-1}, 10 cycles at 15 mAg^{-1}.

For a correct evaluation of the reversibility, the charge efficiency was calculated at 15 mAg^{-1}, as at lower currents the secondary reactions have more time to develop. The MXT-5 and MTX-30 show average efficiencies of 99.74% and 99.56%, respectively, while the capacity retentions are 100% and 95%. To our knowledge, the reversibility of the MXT-5 is the highest reported so far for Na-ion negative electrodes. A full cell has also been assembled using $Na_{0.44}MnO_2$ as positive electrode. The cell exploits the full MXene capacity and it does not suffer of capacity fading after 150 cycles (Figure 1b). The MXT-5 not only has better cycling properties, but also shows a higher rate capability, as already shown by our group, being able to deliver 85 mAhg^{-1} at 1500 mAg^{-1},[13]. It is clear that the electrochemical performance largely depends on the preparation routes, that in turns determine the degree of crystallinity and composition of the samples. It is thus essential to get insight in the short- and long- range structure of the MXene compounds to explain these relevant differences in the functional behavior. Hereafter, we propose for the first time a structural model based on building blocks which is supported by the combined analysis of X-ray and neutron diffraction, X-ray absorption spectroscopy (XAS), and high-resolution transmission electron microscopy (HRTEM) measurements. The model was firstly validated on the MAX precursor, considered as starting point for the definition of the structural building blocks.

Despite the large abundancy of diffraction data of MXenes, their quantitative analysis is an open challenge, and the crystal structure of the MXene is still unresolved. Highly crystalline samples have been obtained only with specific techniques (*e.g.* epitaxial thin film[25,26,27]), but powdered

materials are poorly crystalline[2,20]. The patterns reported in literature are always characterized by features associated with the MAX precursor (space group $P6_3/mmc$) as some reflections are characteristic of both the systems[1,13,21,22]. The atomic arrangements of the Ti_3AlC_2 and $Ti_3C_2T_x$ phases are depicted in Figure 2. The detailed description of the synthesis and the structural features are reported in the SI-Section 1,2 together with a brief overview of the literature. The MXene structure is strongly related to that of the MAX phase as it is obtained by the removal of the A layer with the subsequent insertion of the T terminations (Figure 2a,b)[28-32].
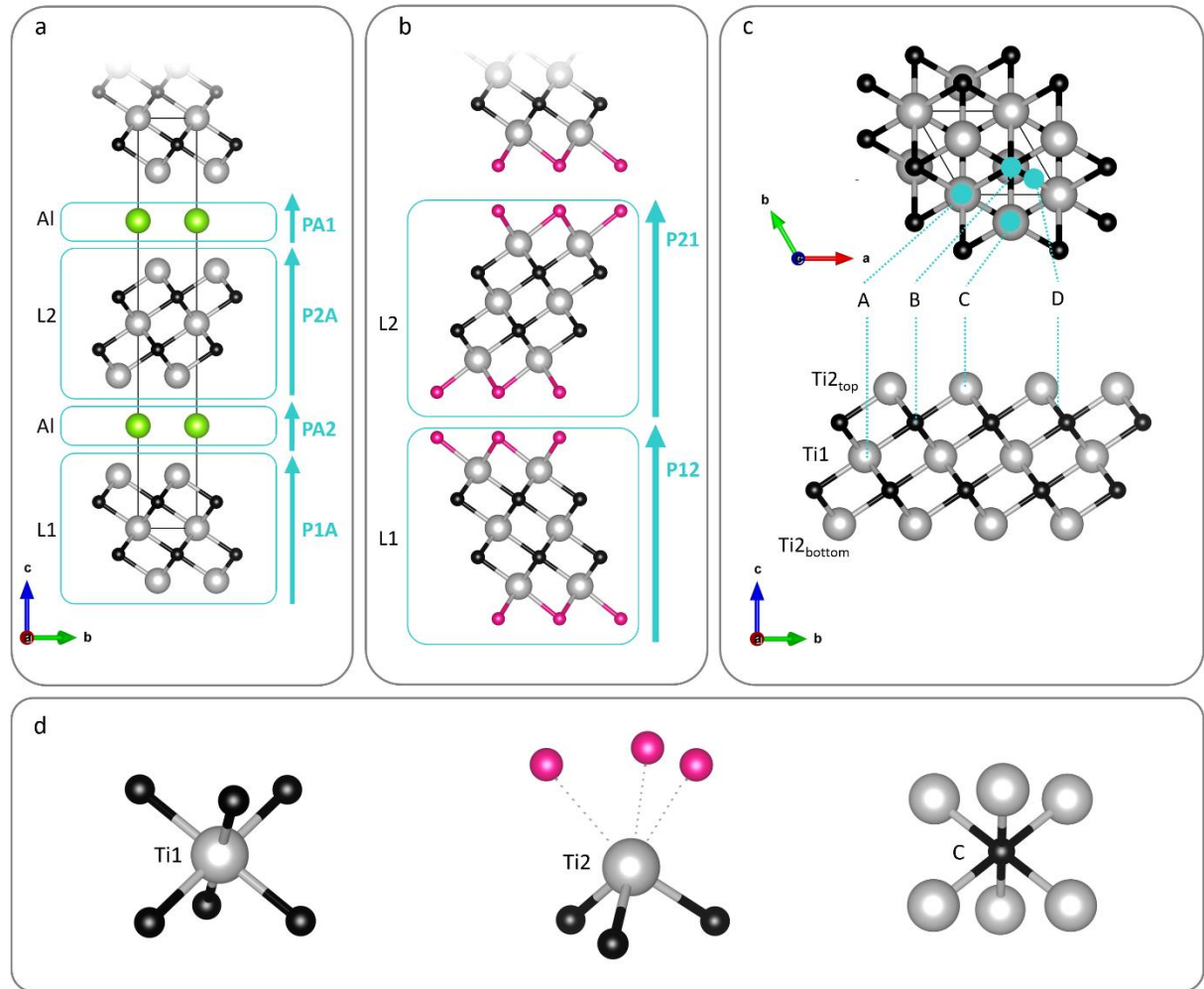

Figure 2. Picture of Ti_3AlC_2 and $Ti_3C_2T_x$ (Ti grey, C black, Al green, T pink. a) Ti_3AlC_2 MAX phase layered structure (SG P6$_3$/mmc). In Faults description, the layered structure (…L1- Al - L2- Al…) is defined by the stacking probability vectors P1A, PA2, P2A, PA1 (light blue arrows); b)

Ti$_3$C$_2$T$_2$ MXene layered structure derived from the MAX phase. In Faults descriptions, the stacking sequence of layers (…L1-L2-L1..) is defined by the stacking probability vectors P12 and P21 (light blue arrows); c) A,B,C,D termination sites derived from previous studies[28-32]: Site A is aligned with the vertical projection over the Ti1 site; site B is on the top of the carbon site; site C is on the top of the Ti2 site; site D (defined also as "bridging") is halfway between the Ti2 and carbon sites; d) schematic representation of the first neighbor shell for Ti1, Ti2, and carbon sites. For Ti1 and carbon sites the positions of the nearest neighbors are defined, for the Ti2 site the location of the terminations (marked with dotted lines) is unclear. In the present scheme the terminations are reported on the less energetic site (A) according to literature[28-30].

The analogies and the differences between the two systems can be also inferred from the relative diffraction patterns, as reported in Figure 3 and Figure S1. For the MAX phase a complete indexing of the pattern is possible; on the contrary for the MXenes only the 00l and the 110 reflections are identified in analogy with the MAX phase. The shift to lower angles of the 002 reflection (generally observed in the 7°-11° range, Cu-K$_\alpha$ radiation) has been used to monitor the variation of the interlayer distance due to the replacement of the A element with the terminations and the possible intercalation of ions/molecules. While the others MXT 00l reflections are often clearly visible and resolved, the reflections in the 30-50° angular range (X-ray, Cu-K$_\alpha$ radiation) are blurred and merged in a single unresolved diffraction band (Figure 4a,b) which is always observed for the Ti$_3$C$_2$T$_x$ compositions and other MXenes[4,21,33]. Careful comparison among several studies shows that different preparation routes lead to a different degree of broadening and merging which was related to structural disorder only qualitatively and has never quantitatively addressed.

Here, for the first time to our knowledge, we proposed a complete analysis of the diffraction patterns, based on the recently proposed approach embodied in the Faults software, which describes the structure without using a space group but instead introducing layers with associated stacking vectors and vector probability[34,35]. This approach has been successfully used for the description of layered and non-layered materials for energy storage applications[36,37,38]. In order to validate this approach, we first analyzed the diffraction patterns of the MAX phase and the obtained results were compared with those derived from conventional Rietveld refinement (see SI Section 3, Figure S1 and Table S1). The stacking sequence of the MAX composition can be described as a sequence of -L1-Al-L2-Al- units with the same connectivity but different orientation (see Figure 2a). The composition, structure, and relative orientation of each layer can be easily derived from the traditional space group-based description. The results of Faults minimization are reported in Figure 2, Figure 3, and Figure S1 for neutron and X-Ray diffraction data, and, based on the evaluation of the agreement factors, it is evident that the traditional Rietveld refinement (Figure S1) and the Faults minimization give equivalent description of the structure of the MAX phase, and the phase composition at the end of the synthetic path (see Table S1 and Figure S1). In particular, neutron powder diffraction data have been exploited as more sensitive to light atoms and thus allows for refinement of atomic position and relative occupancies of terminations sites.

The Faults approach offers the possibility to evaluate the presence of extended defects such as stacking faults, antiphase domains or intergrowths. The presence of stacking faults can be explored moving the value of the stacking vector out of the equilibrium value (*i.e.* the perfect crystal structure): attempts to refine this parameter led to its original value. The presence of different stacking sequences (L1-Al-L1-Al, L2-Al-L2-Al, L1-L1, L1-L2) and of layers of the

lower and higher order MAX phases (Ti_2C and Ti_4C_3) have been considered, being the spark plasma sintering (SPS) synthesis compatible with the formation of such defects. The initial probability value of each defect was set equal to 10%; all the refinements lead to negligible probability values. Based on these results, the presence of significant levels of extended defects in the MAX sample can be excluded, in good agreement with a previous report describing the MAX system as a layered compound with the maximum possible degree of ordering (MPDO)[39].
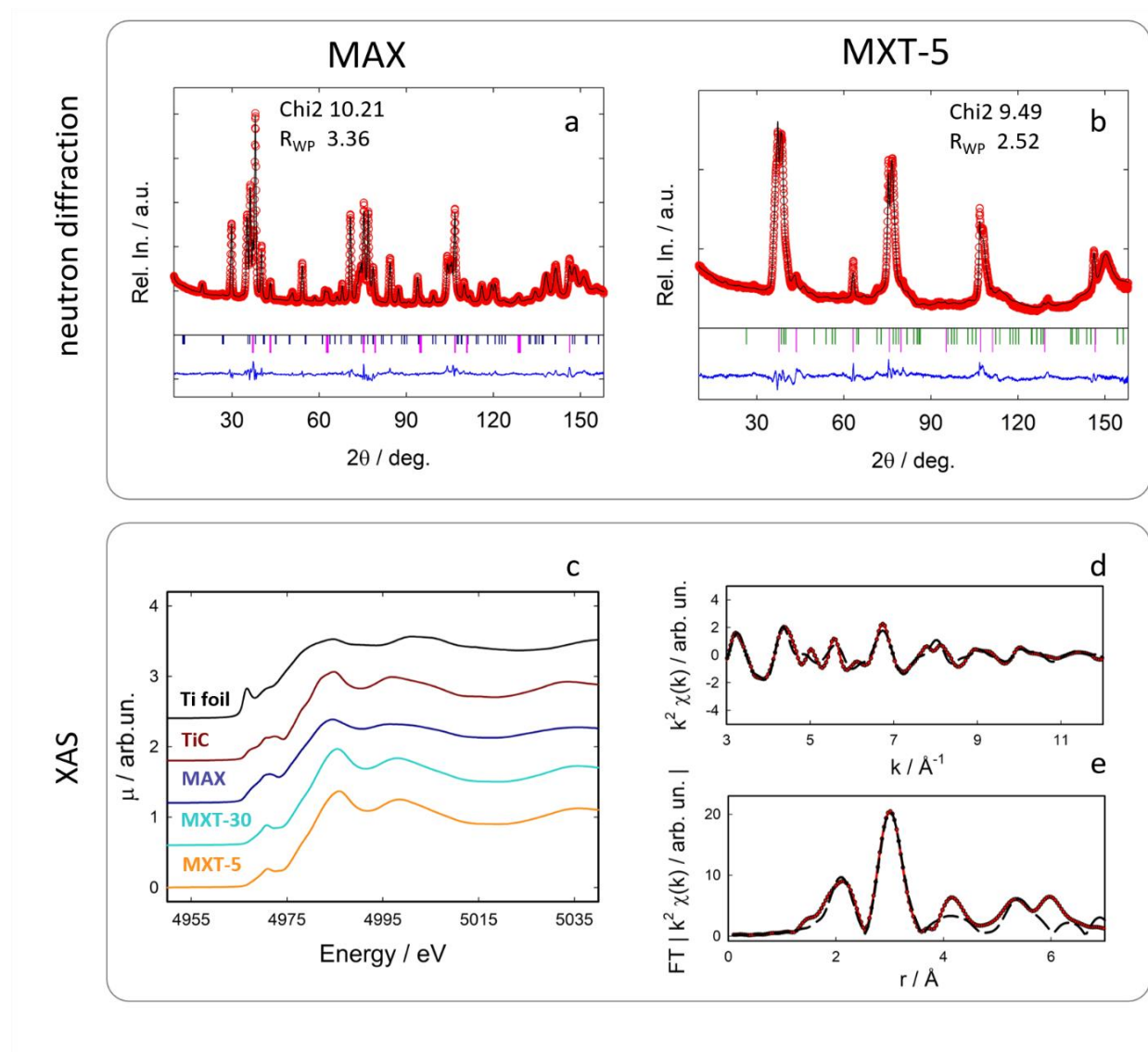
Figure 3. Neutron diffraction patterns for the (a) MAX and (b) MXT samples together with the results of Faults minimization and agreement factors (experimental data: red dots, calculated patterns black lines, difference functions: blue lines). Vertical bars are related to impurities: TiC pink, Ti_2AlC blue, TiO_2 green. (c) XANES spectra at the Ti K-edge for metallic Ti foil, TiC, MAX phase, MXT-5 and MXT-30. All the spectra are shifted along the y-axis for better clarity. The direct comparison of the spectra of MAX and MXT-5, without any vertical shift, can be found in the SI, Figure S2. (d) EXAFS signal and corresponding (e) Fourier Transform (FT) of MXT-5 (experimental data: red lines, simulated curves (Model A): black dotted lines).

The MXene structure, as discussed in SI Section 2 and 4, is characterized by structural anisotropy with respect to the MAX precursor due to the strong, covalent Ti-C bonds within the 2D blocks and the weak van der Waals interactions between the blocks, as confirmed by the increased interlayer distance d_{002} obtained by the diffraction patterns, shown in Figure 3 and Figure 4. More important, MXenes obtained under different experimental conditions present a different degree of disorder (Section 2-SI), as highlighted by experimental evidence (Section 4-SI). Thus, a high amount of point defects on the layer surface (atomic displacements, vacancies, substitutions on the termination sites), and of two- dimensional defects (stacking faults) can be expected. The presence of such defects is favored by the weak interactions among the layers, resulting in different stacking configurations with very similar energies. The MXene morphology is generally dominated by this effect, and lamellae or small particles in form of platelets are observed[4,13,21].

In order to decrease the number of free parameters of the structural model, we first investigated the MXT-5, MXT-30, and MAX local electronic and atomic structure through XAS at the Ti K-edge. The XANES (X-ray absorption near edge structure) spectra are shown in Figure 3. The

spectrum of the MAX phase displays a close resemblance to that of TiC and a close edge-energy position. Conversely, the spectrum of both the MXene compositions is shifted to higher energies of *ca.* 1.5 eV with respect to Ti_3AlC_2, indicating a lower electron density on Ti due to the formation of bonds with electronegative atoms (F, O), in nice agreement with our previous results [13]. The edge energy position was found to be coincident to Ti_2O_3 (Figure S2), however, due to the intrinsic differences in term of electronic structures between titanium oxides and carbides, a precise assessment of the formal oxidation state close to Ti(III) is only tentative. The pre-edge region is constituted by two peaks, clearly visible for the MAX phase, attributed to the Ti *1s* → C *2p* + Ti *3d* (t_{2g} and e_g) hybridized orbitals[40,41]. The peak at lower energies has a considerably lower intensity for MXene than for the MAX phase, as a consequence of their different electronic structure[42]. Only very slight differences are detected between MTX-5 and MTX-30 around the pre-edge peak (see Figure S2), confirming that their electronic and atomic structure is substantially the same. MTX-5 was then taken as representative for further EXAFS (Extended X-ray absorption fine structure) analysis to investigate the local structure. Three structural models with formula $Ti_3C_2F_2$ were considered (see Figure 3d,e), each composed by a TiC skeleton, but having three different termination positions derived from previous DFT calculations[28-30] (Figure 2c). Model A presents termination F in the A site at 0, 0, *z*, model B in the B site at 2/3, 1/3, *z*, and model C in the C site at 1/3, 2/3, *z*. The best fit was obtained for model A (Figure 3d,e), showing a very nice agreement with the experimental data (F factor equal to 10%, Section 4-SI and Table S2) and with the relative stability obtained from DFT studies[28-31].

The information obtained by XAS, together with the description of the MXene layers and termination configuration, have been considered to build the structural model for the analysis of

the diffraction data for MXT-5 and MXT-30. Details and discussion are reported in Section 4-SI. As already pointed out, indeed, the broadening of the diffraction patterns does not allow the profile matching or Rietveld refinement for both neutron and X-ray diffraction patterns and the analysis here reported has been performed only with the Faults approach. The two building blocks of the MXene structures are the L1 and L2 units (see Figure 2) with associated stacking vectors P12 and P21. Terminal sites have been added in the L1 and L2 blocks, exploring different possibilities. The starting value for the d interlayer spacing was defined by the evaluation of the interplanar distance associated to the position of the 002 reflection and subsequently refined. The d spacing is strictly correlated with the z component of the P12 and P21 stacking vectors that can be thus used as descriptors of the disorder in the structure. The effect of the variation of all the structural parameters (i.e. the positions of atoms M, X, T, the composition, the site occupancy, the stacking vectors and the stacking probability) were evaluated by means of Faults simulation and minimization.

To account for the hk band in the 30°-50° degree range, two major possible sources of disorder have been identified: the distribution of termination sites and the stacking sequence. The relative occurrence of A, B, and C termination sites with mixed F/O occupancies were allowed to vary, and results indicated that the A sites, followed by the B site, are the most represented, while the C occupancy spontaneously reaches negligible values, in excellent agreement with the results from XAS. This was considered as the best starting model for the introduction of stacking faults, whose presence has been considered introducing extra L1 and L2 layers, for which the stacking vectors were moved from the ideal position (0, 0, 0.5); details are given in Section 4-SI. In this case a direct refinement of both X-ray and neutron data have been attempted and results are reported in Figure 3 and Figure 4.
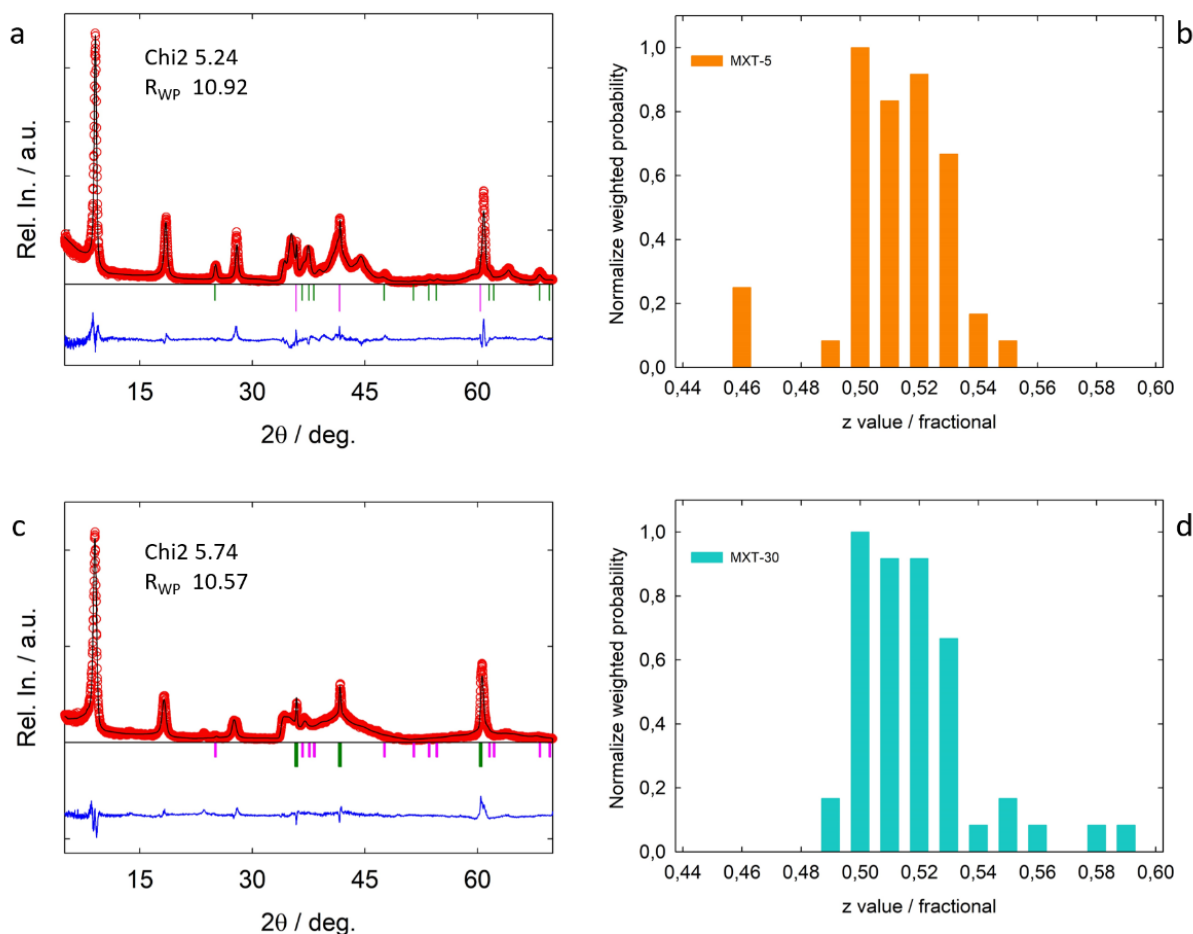
Figure 4. XRD data and Faults fit for the (a) MXT-5, and (c) MXT-30 samples. Normalized weighted population of z components of the stacking vectors P12/P21 for the (b) MXT-5, and /d) MXT-30 obtained from the analysis of the Faults fits.

The obtained results indicate that high levels of disorder are present already in MXT-5, obtained under milder condition[13]. A detailed analysis of the stacking vectors for the most represented sequences reveals that the stacking faults affect for the *xy* and *z* dimensions. In particular, the most represented values for the in-plane sliding are (1/3; 2/3), (2/3; 1/3). Considering that the A termination site is the most populated, this implies that the subsequent layers tend to glide for minimizing the repulsion between facing terminations and to assume an indented interlocked

zipper-like configuration; this kind of dislocation is often associated with z values of the P

stacking vectors < 0.5. This allows for the minimization of the repulsion and leads also to a

reduction of the interlayer distance. The analysis of the z parameters of the refined stacking

vectors are reported in Figure 4 for the MXT-5 and MXT-30 compositions, both characterized by

a wide distribution. The MXT-5 sample is characterized by a minimum and maximum value of

the refined z parameter corresponding to 8.7 Å and 10.3 Å, respectively giving a weighted mean

value equal to 9.5(0.4) Å. The situation is even more extreme for the MXT-30 composition,

presenting a broaden hk band and an even wider distribution of z values of the stacking vector,

with minimum and maximum values of 8.4 Å and 11.2 Å respectively, and a weighted mean

value of 9.8(0.5) Å. From the diffraction point of view, the combined effect of the glide in the xy

plane and the distribution of interlayer distances hinders the coherent scattering among adjacent

layers, resulting in the broadening of the $(10l)$ class of reflection and thus generating the hk band,

characteristic of the MXenes. Thus, while the distribution of the termination sites modulates the

relative intensities of the hk features, the stacking faults determine the size of the broadening.

This scenario is also confirmed by TEM measurements presented in Figure 5b-c for MTX-5 (see

also Figure S6 for MTX-30 and section 1-SI for details on the image analysis). To highlight the

microscopic structure of the flakes along the stacking direction, we have implemented a Fourier

filtering procedure where only the sharp peaks due to the regular $(00l)$ structure were selected to

reconstruct a real space image. The average d_{002} distance is 9.8 Å, which is in excellent agreement

with the results obtained from XRD and neutron diffraction data analysis, and with previous

literature TEM reports[43-45]. A closer inspection of the images shows a variability of such distance

not only among different layers, but also for the same neighboring layers along different spatial

regions, especially at the edges of the MXene flakes, a situation which is more severe, from a

qualitative point of view, for MTX-30 (Figure S6). A wide range of previously reported HRTEM images for $Ti_3C_2T_x$ samples obtained under similar synthetic conditions[43,46] or as thin films and single layer[26,31] show the same morphological features. Again, the d_{002} variability is associated to the nature and distribution of the terminations. Facing terminations between adjacent layers will lead to an expanded d_{002} to reduce the repulsion, while indented positions are compatible with lower d_{002} values. The actual presence of residual H_2 or H_2O molecules from the synthesis can also affect the d_{002} distance, as also evaluated theoretically[29].

To conclude, the present study identifies the origin of the structural disorder in $Ti_3C_2F_{1-x}O_x$ MXenes in the distribution of termination on A and B sites and in the presence of dislocations. The z component of the stacking vector can be used as a quantitative descriptor of the structural disorder, and it can be used to discriminate between MXene compositions obtained under different synthetic conditions. The variation of the HF concentration in the etching stage of the synthesis acts directly on the degree of disorder, modulating the distribution of the observed d spacing values. The higher the concentration, the fastest the etching reaction, the broader the distribution of the observed d values. A narrower distribution of the z values is beneficial for the long cycling capability of the materials and allows capacity retention values of 100% for hundreds of cycles.
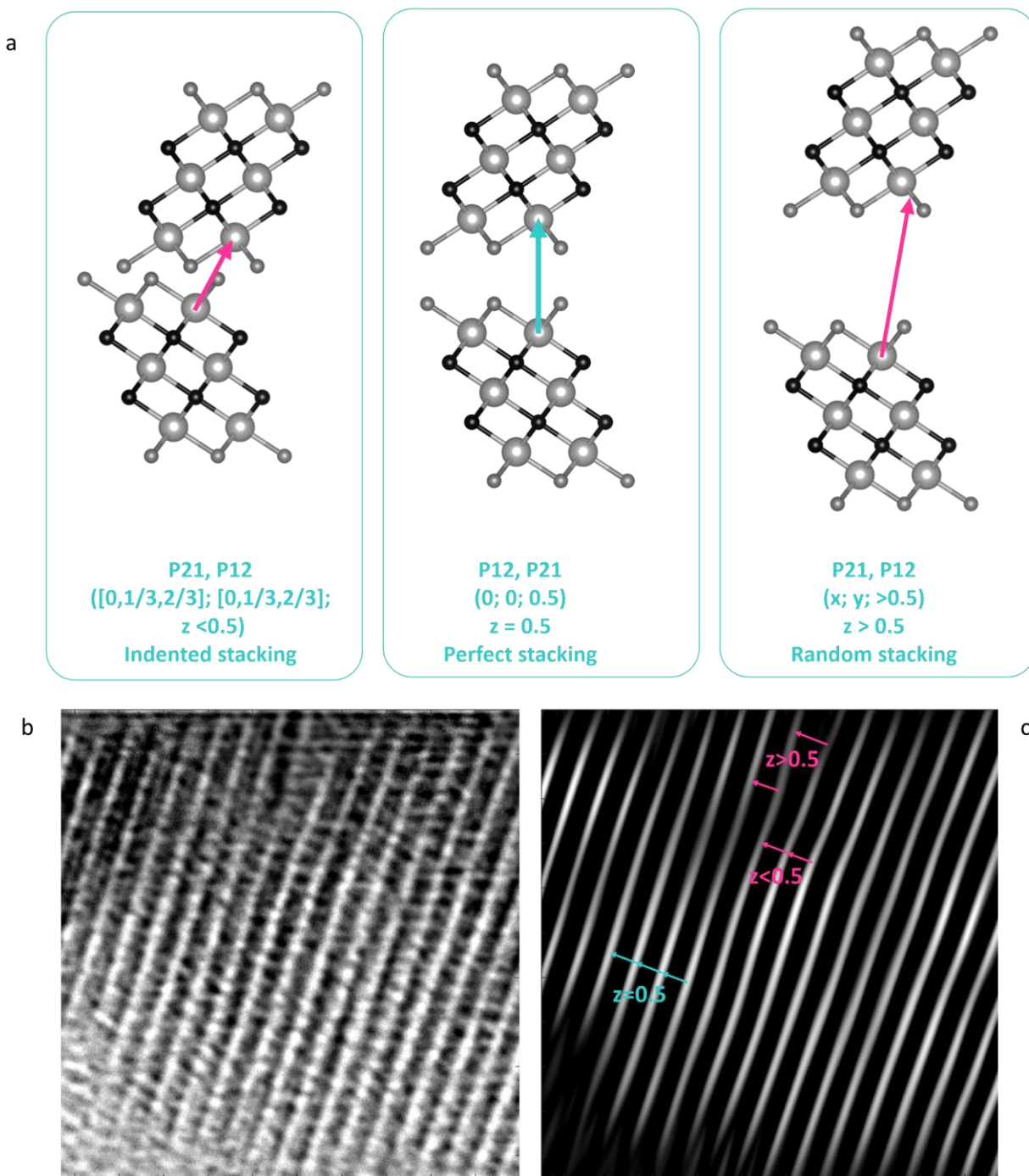
Figure 5. (a) Schematic representation of the most represented type of disorder depending on the observed value for the z component of the stacking vector. The $z = 0.5$ represents the ideal crystal situation with the Ti1 of one layer directly facing the Ti1 of the adjacent layer (see arrow in the central panel). When $z < 0.5$, to minimize the repulsion among the termination the sliding of adjacent layers of (*1/3; 0*) (*2/3,0*) (*0, 1/3*), (*0, 2/3*) favor the indented configuration of facing Ti1

atoms. On the contrary, when $z > 0.5$ the loosening of the weak interactions leads to random sliding in x, y direction of the adjacent layers. This type of defects can be detected in the TEM images obtained for the MXT-5 (b) TEM image of MTX-5, the picture shows a 17x17 nm area of the sample perpendicular to the c axis; (c) Fourier filtered TEM image of MTX-5, the picture shows the same area of the TEM image.

Supporting Information.

The following files are available free of charge. SI (PDF file) includes a brief discussion on the MAX and MXT structure, synthesis, and previous literature results on the structural characterization. Information on the experimental methods and measurements are described. Details and results from the XAS analysis, Rietveld refinement and models, Faults minimization and simulations, building blocks for the MXene structure and additional TEM images are also given.

Corresponding Author

*Riccardo Ruffo, Materials Science Department, University of Milano-Bicocca, via Cozzi 55, 20125 Milano, Italy. e-amil: riccardo.ruffo@unimib.it

Author Contributions

The manuscript was written through contributions of all authors. All authors have given approval to the final version of the manuscript.

Funding Sources

REFERENCES

(1) B. Anasori, Y. Gogotsi, 2D Metal Carbides and Nitrides (MXenes), © Springer Nature Switzerland, **2019**.

(2) Y. Gogotsi, B. Anasori, The Rise of MXenes, *ACS Nano*. **2019**, *13* (8), 8491–8494.

(3) J. Haemers, R. Gusmão, Z. Sofer, Synthesis Protocols of the Most Common Layered Carbide and Nitride MAX Phases, *Small Methods* **2020**, *4* (3), 1–32.

(4) M. Naguib, M. Kurtoglu, V. Presser, J. Lu, J. Niu, M. Heon, L. Hultman, Y. Gogotsi, M.W. Barsoum, Two-Dimensional Nanocrystals Produced by Exfoliation of Ti_3AlC_2, *Adv. Mater.* **2011**, *23* (37), 4248–4253.

(5) C. Ferrara, A. Gentile, S. Marchionna, R. Ruffo, $Ti_3C_2T_x$ MXene compounds for electrochemical energy storage, *Curr. Opin. Electrochem*. **2021**, *29*, 100764.

(6) Z. Li, Y. Wu, 2D Early Transition Metal Carbides (MXenes) for Catalysis, *Small* **2019**, *15*, 1804736.

(7) Q. Hu, D. Sun, Q. Wu, H. Wang, L. Wang, B. Liu, A. Zhou, J. He, MXene: A new family of promising hydrogen storage medium, *Phys. Chem. A* **2013**, *117* (51), 14253–14260.

(8) A. Sinha, Dhanjai, H. Zhao, Y. Huang, X. Lu, J. Chen, R. Jain, MXene: An emerging material for sensing and biosensing, *TrAC - Trends Anal. Chem*. **2018**, *105*, 424–435.

(9) L.M. Dong, C. Ye, L.L. Zheng, Z.F. Gao, F. Xia, Two-dimensional metal carbides and nitrides (MXenes): preparation, property, and applications in cancer therapy, *Nanophotonics* **2020**, *9*, 2125–2145.

(10) S.K. Hwang, S.M. Kang, M. Rethinasabapathy, C. Roh, Y.S. Huh, MXene: An emerging two-dimensional layered material for removal of radioactive pollutants, *Chem. Eng. J.* **2020**, *397*, 125428.

(11) X. Xu, Y. Zhang, H. Sun, J. Zhou, F. Yang, H. Li, H. Chen, Y. Chen, Z. Liu, Z. Qiu, D. Wang, L. Ma, J. Wang, Q. Zeng, Z. Peng, Progress and Perspective: MXene and MXene-Based

Nanomaterials for High-Performance Energy Storage Devices, *Adv. Electron. Mater*. **2021**, *7* (7), 2000967.

(12) M. Naguib, J. Come, B. Dyatkin, V. Presser, P.L. Taberna, P. Simon, M.W. Barsoum, Y. Gogotsi, MXene: A promising transition metal carbide anode for lithium-ion batteries, *Electrochem. Commun*. **2012**, *16*, (1), 61–64.

(13) A. Gentile, C. Ferrara, S. Tosoni, M. Balordi, S. Marchionna, F. Cernuschi, M.H. Kim, H.W. Lee, R. Ruffo, Enhanced Functional Properties of $Ti_3C_2T_x$ MXenes as Negative Electrodes in Sodium-Ion Batteries by Chemical Tuning, *Small Methods* **2020**, *4* (9), 2000314.

(14) Y. Wu, Y. Sun, J. Zheng, J. Rong, H. Li, L. Niu, MXenes: Advanced materials in potassium ion batteries*, Chem. Eng. J*. **2021**, *404*, 126565.

(15) M.K. Aslam, Y. Niu, M. Xu, MXenes for Non-Lithium-Ion (Na, K, Ca, Mg, and Al) Batteries and Supercapacitors, *Adv. Energy Mater*. **2020**, *11* (2), 2000681.

(16) X. Chen, Y. Zhao, L. Li, Y. Wang, J. Wang, J. Xiong, S. Du, P. Zhang, X. Shi, J. Yu, MXene/Polymer Nanocomposites: Preparation, Properties, and Applications, *Polym. Rev*. **2021**, *61* (1), 80–115.

(17) F. Song, G. Li, Y. Zhu, Z. Wu, X. Xie, N. Zhang, Rising from the horizon: three-dimensional functional architectures assembled with MXene nanosheets, *J. Mater. Chem. A*. **2020**, *8*, 18538–18559.

(18) F. Bu, M.M. Zagho, Y. Ibrahim, B. Ma, A. Elzatahry, D. Zhao, Porous MXenes: Synthesis, structures, and applications, *Nano Today*. **2020**, *30*, 100803.

(19) T. Rackl, D. Johrendt, The MAX phase borides Zr_2SB and Hf_2SB, *Solid State Sci*. **2020**, *106*, 106316.

(20) M. Alhabeb, K. Maleski, B. Anasori, P. Lelyukh, L. Clark, S. Sin, Y. Gogotsi, Guidelines for Synthesis and Processing of Two-Dimensional Titanium Carbide ($Ti_3C_2T_x$ MXene), *Chem. Mater*. **2017**, *29* (18) 7633–7644.

(21) T. Li, L. Yao, Q. Liu, J. Gu, R. Luo, J. Li, X. Yan, W. Wang, P. Liu, B. Chen, W. Zhang, W. Abbas, R. Naz, D. Zhang, Fluorine-Free Synthesis of High-Purity $Ti_3C_2T_x$ (T=OH, O) via Alkali Treatment, *Angew. Chemie* **2018**, *57* (21), 6115–6119.

(22) X. Li, M. Li, Q. Yang, G. Liang, Z. Huang, L. Ma, D. Wang, F. Mo, B. Dong, Q. Huang, C. Zhi, In Situ Electrochemical Synthesis of MXenes without Acid/Alkali Usage in/for an Aqueous Zinc Ion Battery, *Adv. Energy Mater*. **2020**, *10* (36), 202001791.

(23) J.Y. Hwang, S.T. Myung, Y.K. Sun, Sodium-ion batteries: Present and future, *Chem. Soc. Rev.* 2017, *46*, 3529–3614.

(24) X. Wang, S. Kajiyama, H. Iinuma, E. Hosono, S. Oro, I. Moriguchi, M. Okubo, A. Yamada, Pseudocapacitance of MXene nanosheets for high-power sodium-ion hybrid capacitors, *Nat. Commun*. **2015**, *6*, 6544.

(25) J. Halim, M.R. Lukatskaya, K.M. Cook, J. Lu, C.R. Smith, L.Å. Näslund, S.J. May, L. Hultman, Y. Gogotsi, P. Eklund, M.W. Barsoum, Transparent conductive two-dimensional titanium carbide epitaxial thin films, *Chem. Mater*. **2014**, *26* (7), 2374–2381.

(26) J. Halim, I. Persson, E.J. Moon, P. Kühne, V. Darakchieva, P.O.Å. Persson, P. Eklund, J. Rosen, M.W. Barsoum, Electronic and optical characterization of 2D Ti_2C and Nb_2C (MXene) thin films, *J. Phys. Condens. Matter*. **2019**, *31* (16), 165301.

(27) M. Benchakar, L. Loupias, C. Garnero, T. Bilyk, C. Morais, C. Canaff, N. Guignard, S. Morisset, H. Pazniak, S. Hurand, P. Chartier, J. Pacaud, V. Mauchamp, M.W. Barsoum, A. Habrioux, S. Célérier, One MAX phase, different MXenes: A guideline to understand the crucial role of etching conditions on $Ti_3C_2T_x$ surface chemistry, *Appl. Surf. Sci.* **2020**, *530*, 147209.

(28) T. Hu, M. Hu, B. Gao, W. Li, X. Wang, Screening Surface Structure of MXenes by High-Throughput Computation and Vibrational Spectroscopic Confirmation, *J. Phys. Chem. C*. **2018**, *122* (32), 18501–18509.

(29) Q. Tang, Z. Zhou, P. Shen, Are MXenes promising anode materials for Li ion batteries? Computational studies on electronic properties and Li storage capability of Ti_3C_2 and $Ti_3C_2X_2$ (X = F, OH) monolayer, *J. Am. Chem. Soc*. **2012**, *134* (40), 16909–16916.

(30) M. Naguib, V.N. Mochalin, M.W. Barsoum, Y. Gogotsi, 25th anniversary article: MXenes: A new family of two-dimensional materials, *Adv. Mater*. **2014**, *26* (7), 992–1005.

(31) C. Zhan, W. Sun, Y. Xie, D.E. Jiang, P.R.C. Kent, Computational Discovery and Design of MXenes for Energy Applications: Status, Successes, and Opportunities, *ACS Appl. Mater. Interfaces*. **2019**, *11* (28), 24885–24905.

(32) L.H. Karlsson, J. Birch, J. Halim, M.W. Barsoum, P.O.Å. Persson, Atomically Resolved Structural and Chemical Investigation of Single MXene Sheets, *Nano Lett*. **2015**, *15* (8), 4955–4960.

(33) J. Michael, Z. Qifeng, W. Danling, Titanium carbide MXene: Synthesis, electrical and optical properties and their applications in sensors and energy storage devices, *Nanomater. Nanotechnol.* **2019**, *9*, 1–9.

(34) M. Casas-Cabanas, M. Reynaud, J. Rikarte, P. Horbach, J. Rodríguez-Carvajal, FAULTS: A program for refinement of structures with extended defects, *J. Appl. Crystallogr*. **2016**, *49*, 2259–2269.

(35) M. Casas-Cabanas, J. Rodríguez-Carvajal, J. Canales-Vázquez, Y. Laligant, P. Lacorre, M.R. Palacín, Microstructural characterisation of battery materials using powder diffraction data: DIFFaX, FAULTS and SH-FullProf approaches, *J. Power Sources*. **2007**, *174* (2), 414–420.

(36) K. Asakura, S. Okada, H. Aral, S.I. Tobishima, Y. Sakurai, Cathode properties of layered structure Li_2PtO_3, *J. Power Sources.* **1999**, *81–82*, 388–392.

(37) C. Delmas, C. Tessier, Stacking faults in the structure of nickel hydroxide: A rationale of its high electrochemical activity, *J. Mater. Chem*. **1997**, *7* (8), 1439–1443.

(38) R. Shunmugasundaram, R.S. Arumugam, J.R. Dahn, A study of stacking faults and superlattice ordering in some Li-rich layered transition metal oxide positive electrode materials, *J. Electrochem. Soc*. **2016**, *163*, A1394–A1400.

(39) B. Lanson, Modelling of X-ray diffraction profiles: Investigation of defective lamellar structure crystal chemistry, *Layer. Miner. Struct. Their Appl. Adv. Technol*. **2012**, *11*, 151–202.

(40) M.R. Lukatskaya, S.M. Bak, X. Yu, X.Q. Yang, M.W. Barsoum, Y. Gogotsi, Probing the Mechanism of High Capacitance in 2D Titanium Carbide Using in Situ X-Ray Absorption Spectroscopy, *Adv. Energy Mater*. **2015**, *5* (15), 1500589.

(41) Y. Xie, M. Naguib, V.N. Mochalin, M.W. Barsoum, Y. Gogotsi, X. Yu, K.W. Nam, X.Q. Yang, A.I. Kolesnikov, P.R.C. Kent, Role of surface structure on li-ion energy storage capacity of two-dimensional transition-metal carbides, *J. Am. Chem. Soc*. **2014**, *136* (17), 6385–6394. doi:10.1021/ja501520b.

(42) M. Magnuson, M. Mattesini, Chemical bonding and electronic-structure in MAX phases as viewed by X-ray spectroscopy and density functional theory, *Thin Solid Films*. **2017**, *621*, 108–130.

(43) Y. Dong, Z. Wu, S. Zheng, X. Wang, J. Qin, S. Wang, X. Shi, X. Bao, Ti_3C_2 MXene-Derived Sodium/Potassium Titanate Nanoribbons for High-Performance Sodium/Potassium Ion Batteries with Enhanced Capacities *ACS Nano* **2017**, 11 (5), 4792–4800.

(44) X. Wang, X. Shen, Y. Gao, Z. Wang, R. Yu, L. Chen, Atomic-scale recognition of surface structure and intercalation mechanism of Ti_3C_2X, *J. Am. Chem. Soc*. **2015**, *137* (7), 2715–2721.

(45) W.H.K. Ng, E.S. Gnanakumar, E. Batyrev, S.K. Sharma, P.K. Pujari, H.F. Greer, W. Zhou, R. Sakidja, G. Rothenberg, M.W. Barsoum, N.R. Shiju, The Ti_3AlC_2 MAX Phase as an Efficient Catalyst for Oxidative Dehydrogenation of n-Butane, *Angew. Chemi* **2018**, *57* (6), 1485–1490.

(46) A. Rosenkranz, P.G. Grützmacher, R. Espinoza, V.M. Fuenzalida, E. Blanco, N. Escalona, F.J. Gracia, R. Villarroel, L. Guo, R. Kang, F. Mücklich, S. Suarez, Z. Zhang, Multi-layer $Ti_3C_2T_x$-nanoparticles (MXenes) as solid lubricants – Role of surface terminations and intercalated water, *Appl. Surf. Sci.* **2019**, *494*, 13–21.